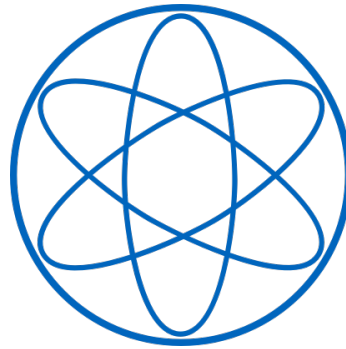LEHRSTUHL FÜR EXPERIMENTELLE
ASTROTEILCHENPHYSIK, E15
PHYSIK - DEPARTMENT

Preparation for the Measurement of ^{53}Mn in an Antarctic Snow Sample
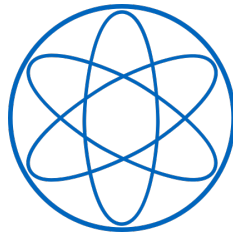
Master's Thesis

DAVID KRIEG

TECHNISCHE UNIVERSITÄT MÜNCHEN

TECHNISCHE UNIVERSITÄT MÜNCHEN

Fakultät für Physik
Lehrstuhl für Experimentelle
Astroteilchenphysik, E15

Master's Thesis

Preparation for the Measurement of ^{53}Mn in an Antarctic Snow Sample

Author:	David Krieg
Supervisor:	Prof. Dr. Stefan Schönert
Advisor:	Dr. Gunther Korschinek
Submission Date:	March 28, 2018

I confirm that this master's thesis is my own work and I have documented all sources and material used.

Munich, March 28, 2018   David Krieg

Abstract

^{53}Mn is a long lived radionuclide with a half life of $t_{\frac{1}{2}} = 3.7 \times 10^6 a$ produced outside Earth's atmosphere by spallation of protons on natural Iron and Nickel in Interplanetary Dust. Measuring the amount of ^{53}Mn in snow samples collected in Antarctica, where terrestrial atmospheric input is minimized, will help to determine Earth's accretion rate of Interplanetary Dust Particles (IDPs). This can be done by linking the measured amount of ^{53}Mn to a model for the ablation of IDPs in the atmosphere (CABMOD), an atmospheric model of deposition for Iron from Micro Meteorites (MMs) and the precipitation rate at the location the samples were recovered.

In this thesis the necessary preparations for this measurement by Accelerator Mass Spectrometry (AMS) at the Maier Leibnitz Laboratory (MLL) are made and calculations for the expected value are presented. Previous attempts of such a measurement failed due to a high isobaric background by the stable isotope ^{53}Cr. Experiments for a better chemical suppression of Chromium in the sample preparation were done in collaboration with the Atom Institute of the Technical University of Vienna. The results of these experiments are shown and discussed.

Contents

Chapter 1

Introduction

Interplanetary Dust Particles (IDPs) are dust grains, floating in interplanetary space. Earth's accumulation rate of these IDPs is a matter of discussion, ranging from 5 (middle atmosphere measurements) up to 300 (space borne dust detection) tons per day [1]. A new approach for a more precise measurement of this accumulation rate can been made by extracting manganese from $500L$ of antarctic snow collected near the Kohnen station (75°S/0°E, $2892m$ above sea level [2]), and measuring the concentration of ^{53}Mn ($t_{\frac{1}{2}} = 3.7 \times 10^6 a$) with Accelerator Mass Spectrometry (AMS) at the Maier Leibnitz Laboratory (MLL) in Garching (Munich). In Antarctica, optimal conditions are found, as an enhanced deposition rate of IDPs, minimal atmospheric and natural dust, and a conserved precipitation rate meet and make it a promising location for sample collection.

Previous AMS measurements were only able to determine an upper limit of the accumulation rate of ^{53}Mn being in the 10^7 range of atoms$/(cm^2 a)$ [3][4]. This was mainly due to a high isobaric background by the stable isotope ^{53}Cr. Chemical extraction of Manganese has already been optimized for meteorites [5] and is sufficient to determine the ^{53}Mn/^{55}Mn ratio and therefore the amount of ^{53}Mn in those samples. But the chemical Chromium suppression has its limits when it comes to the amount of sample mass of IDPs expected in antarctic snow. For very small sample masses, as expected for IDPs in evaporated antarctic snow, the chromium suppression is not sufficient for the separation of Manganese. An improvement of the chemical separation process is needed, since the isobaric suppression of the AMS setup at the MLL with the Gas filled Analyzing Magnet System (GAMS) is not sufficient to suppress the background. Experiments for smaller sample masses with smaller columns and usage of less acid are made to separate Manganese and Chromium form the IDPs in the molten and evaporated snow sample. Only when enhanced chemical separation techniques and good measurement conditions at the tandem accelerator meet, a improvement in the detection limit of long lived radioactive ^{53}Mn will be made. The determination of the amount of ^{53}Mn in the antarctic snow sample will enable us to reduce the range of Earth's extraterrestrial mass accretion rate found in literature.

The Thesis will cover the following topics:

First the origin of IDPs will be discussed in Chapter 2, with different potential sources as the Oort Cloud (OC), the Kuiper Belt (KB), the Asteroid Main Belt (MB) and comets.

Chapter 3 will cover a model of irradiation and estimate the amount of ^{53}Mn expected in IDPs.

In Chapter 4 the ablation of IDPs entering Earth's atmosphere and the consequences of the atmospheric ablation, mainly happening in the mesosphere at 80 to $120km$ altitude, to the global deposition rate of ^{53}Mn are shown.

Sample origin, collection and transport, as well as the experiments for the improvement of the chemical separation of Manganese and Chromium are explained in Chapter 5. Furthermore the AMS measurement techniques used at the MLL is displayed.

Finally, Chapter 6 shows both the conclusions for the measurement of ^{53}Mn in antarctic snow samples and the outlook for more constrains to already existing models for irradiation of IDPs and the daily extraterrestrial mass input on Earth.

Chapter 2

Origin of Interplanetary Dust Particles

The origin of Interplanetary Dust Particles (IDPs) has long been a field of discussion with different potential sources of dust grains as the Oort Cloud (OC), the Kuiper Belt (KB) and the Main Asteroid Belt (MB), with their dust grains being moved by Poynting Robertson (PR) drag [6] towards the Sun and different comet families. The PR drag describes the slowing down of dust grains by the radiation of the Sun. This deceleration leads to a spiraling movement towards the Sun (see Fig. 2.1). When reaching Earth's orbit at one astronomical unit $(1AU)$[1] away from the Sun they can be captured by Earth. While in the nineties the Interplanetary Dust Particle Cloud or Zodiacal Cloud (ZC) was thought to manly consist of dust spiraling in from the Main Asteroid Belt between Mars and Jupiter [7] new research favors these particles mainly being of cometary origin [8].

2.1 The Kuiper Belt and the Oort Cloud Contribution to the Zodiacal Cloud

The Kuiper Belt (KB) is found between the orbit of Neptune and Pluto at a distance of 30 to $50AU$ from the Sun. With estimated 10^5 objects with a diameter larger than $100km$, its population is three orders of magnitude larger than that of the MB [13]. The dust production rate of the KB was estimated to be $8.6 \times 10^4 g/s$ to $2.9 \times 10^7 g/s$ for particles with a diameter smaller $10\mu m$ [14] with 20% able to reach the inner solar system [15]. But since KB dust grains have high eccentricities and inclinations with high encounter velocities Earth's cross section to those particles is relativly small and therefore the KB only accounts for $1 - 2\%$ of the IDPs found on Earth [13].Therefore the KB's contribution to IDPs collected on Earth will be neglected.

The bulk of grains seen in the ZC has a size distribution between $1 - 100\mu m$ [16][17] (see Fig. 2.3). Particles this size originating from the OC in the outer solar system

---

[1]The astronomical unit AU is the distance between the Sun and Earth $\approx 14.9 \times 10^9 m$
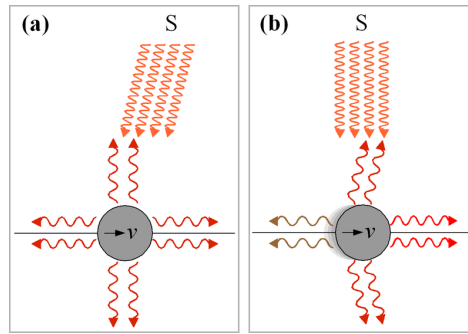
Figure 2.1: Schematic depiction of the PR effect in two different reference frames [9]. Isotropic radiation of the particle is assumed. a) Shows the effect with the moving particle as reference frame. Due to aberration the radiation pressure hits the particle from a forward angle slowing it down. b) Shows the effect with an observer as center of the reference frame. Here the particles movement is decelerated by aberration of the particles radiation.

and beyond are subjected to gas in the interstellar medium (IMS), coulomb drag from ionized components of the ISM and the Lorentz force from the magnetic field of the ISM, and the electric force by the induction electric field from the IMS [18]. This leads to these particles having unbound trajectories and therefore leaving our solar system [18]. The potential contribution of dust particles originating from the OC to the ZC and therefore the IDPs found on Earth is also negligible.

2.2 The Main Belt Contribution to the Zodiacal Cloud

Catastrophic events occurring in the MB were thought to be the main source of IDPs for a long time, with a cometary contribution of only about 20%. These results were supported by IDPs collected from the stratosphere [7][19]. Most of the IDPs ablate completely in the mesosphere (as further explained in Chapter 4.1). Asteroidal dust grains have slower encounter velocities with Earth than cometary ones, which makes them more likely to survive traveling through the atmosphere [8]. This explains the shift towards asteroidal origin of interplanetary dust particles. For the MB we assume a contribution of around 10% to the Zodiacal Cloud [8] [20].

2.3 Cometary Contribution to the Zodiacal Cloud

The main contributor to the ZC are comets. More than 90% of the IDPs surrounding Earth originate from comets or their spectral analog D-type asteroids [20] (ses Fig. 2.4). A Zodiacal Cloud Model (ZCM) based on the orbital properties and lifetime of comets and asteroids, and the dynamical evolution of dust after ejection, constrained
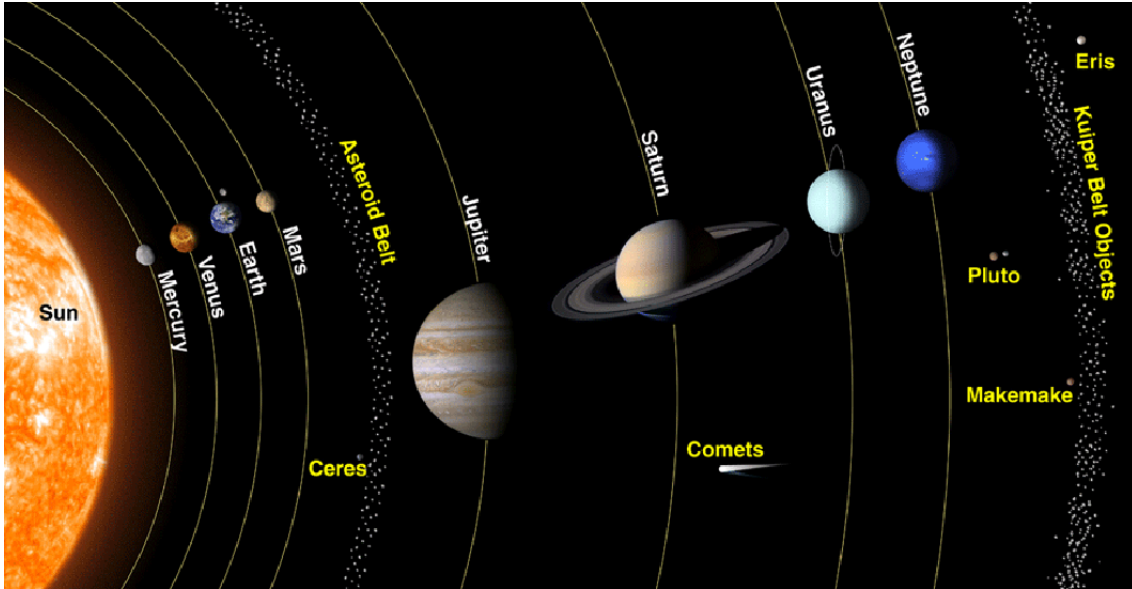
Figure 2.2: Schematic depiction of the solar system [10] with the different regions of origin for IDPs. The distance between Sun and Earth is $1AU$. The MB lies between the orbits of Mars and Jupiter at a distance of $3AU$ from the Sun. Jupiter is around $5AU$ from the Sun. The KB lies beyond Neptune and Pluto at $30-50AU$ from the Sun. The OC stretches out from the KB to more than 10^4AU [11] [12].

by Infrared Astronomical Satellite (IRAS) observations, meteor observations and by properties of recovered micrometeroids (MMs) suggests $85-95\%$ of the IDPs originate from Jupiter Family Comets (JFCs) [8]. The ZCM also suggests that these JFC dust grains make up around 85% of the mass influx on Earth [8]. This would give an explanation to the primitive carbonaceous composition of MMs found in Arctic ice [21].
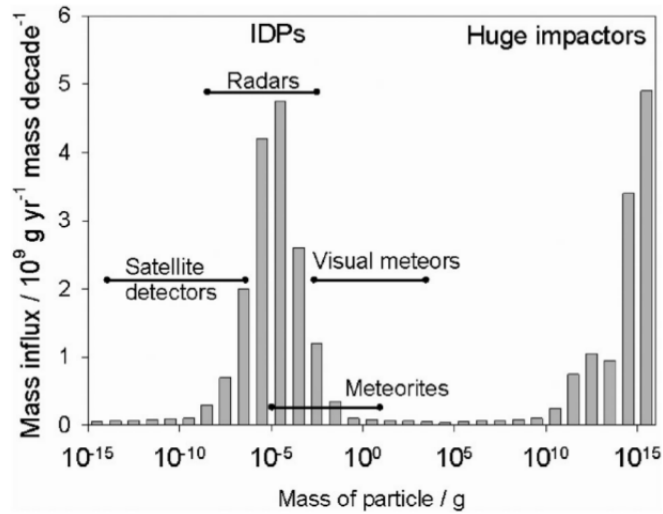
Figure 2.3: Mass influx (per decade of mass) against IDPs mass [1], with different methods used for measuring different mass regions.
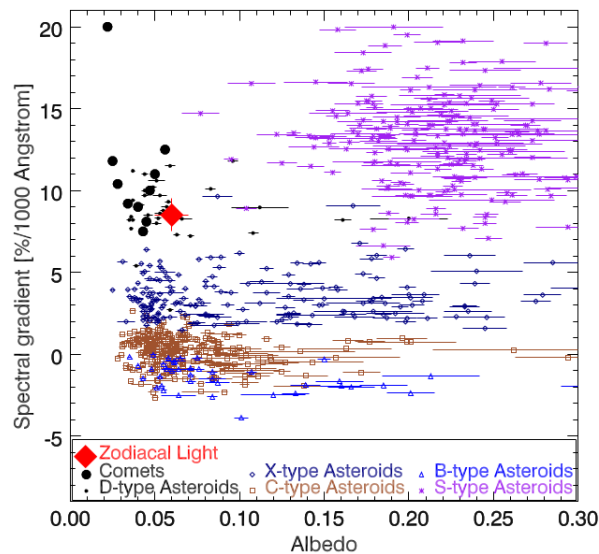
Figure 2.4: Spectral gradient of the Zodiacal Light (ZL) [20], against albedo. ZL is Sunlight reflected form the particles in the ZC. Albedo is a measure of diffuse reflection of Sunlight. It is dimensionless and reaches from 0 for the full absorption case to 1 for full reflection. The spectral gradient describes the dependence of the reflectance of the wave length. Data from different asteroids and comets were plotted with the region of the Zodiacal light. The plot shows that cometary dust dominates the ZC, since the characteristic of the ZL (red) in this graph is located in the cluster of the comets (black).

Chapter 3

^{53}Mn Production in Interplanetary Dust Particles

Interplanetary Dust Particles are exposed to cosmic radiation including solar and galactic cosmic rays (SCRs and GCRs). SCRs originate from the Sun. They mainly consist of protons ($\sim 90\%$). GCRs have their sources outside of the solar system, with their main component also being protons ($\sim 87\%$). The second most abundant particles in SCRs and GCRs are α-particles. Heavier particles, like nuclei, contribute less then 1% [22]. Protons produce a variety of radioactive elements in the IDPs via spallation. The amount of radioactive material produced depends on the irradiation or exposure time, the energy distribution of the protons, the elemental composition of the IDPs and the cross section of the target elements.

^{53}Mn, with a half life of $3.7 Ma$, is produced mainly from two target elements: ^{nat}Fe(p,x)^{53}Mn and ^{nat}Ni(p,x)^{53}Mn [23]. We assume an ordinary chondritic composition of the IDPs [1]. Averaged over the different ordinary chondrite groups a value of $225\frac{mg}{g}$ for ^{nat}Fe and $12.7\frac{mg}{g}$ for ^{nat}Ni is obtained (Tab.3.1) [24]

	H	L	LL	averaged $[\frac{mg}{g}]$
Fe $[\frac{mg}{g}]$	275	215	185	225
Ni $[\frac{mg}{g}]$	16.0	12.0	10.2	12.7

Table 3.1: Mean compositions of the ordinary chondrite group, taken from [24]. The capital letters refer to the subtypes (H: high total Iron and high metallic Iron abundance, L: low total Iron content, LL: low total Iron and metal content). The mean compositions for Iron and Nickel are given and the average is calculated in the last column.

The life time and therefore the exposure time of cometary dust particles was simulated do be $2.5 \times 10^6 a$ [25] and therefore shorter than their Poynting Rbertson (PR) lifetime [25]. The PR effect describes the deceleration of small particles by radiation pressure of solar rays [26]. This deceleration leads to a spiral movement towards the Sun (see Chapter 2). The PR lifetime is the time a particle needs to

reach Earth's orbit to be captured by Earth due to the PR effect causing a drag towards the Sun. The simulated lifetime of cometary particles $(2.5 \times 10^6 a)$ will be taken as a lower limit to the exposure time of IDPs originating from comets, since cometary dust is likely to be trapped in orbital resonances by big planets (especially Jupiter, at $5AU$) [27]. So IDPs from comets reaching Earth's orbit have traveled for a longer time than their average life time calculated by Yang et al. [25] since in this model resonances are not included. As an upper time limit, the Poynting Robertson lifetime of a particle leaving a resonance and spiraling inwards from 5 to $1AU$ (Jupiter to Earth) of $4.4 \times 10^6 a$ is taken. This still does not account for the time the particle was trapped in the resonance. For a reference in between the Poynting Robertson lifetime of a particle set free at a distance of $3AU$ (where the MB is located) and traveling to Earth's orbit at $1AU$, around $10^6 a$ is taken.

The orbital distance from the Sun by the Poynting Robertson effect is given by the equation [28]:

$$\frac{da(t)}{dt} = \frac{-k}{a\rho r} \tag{3.1}$$

Where k is a constant with the value $1.3 \times 5.12 \times 10^{11} \frac{g}{s}$ (for a derivation of this constant please refer to [19]), ρ the density of the particle and r its radius. Considering boundary condition $a(t=0) = a_0 = 3AU$ or respectively $5AU$ (MB or Jupiter), the integration of equation 3.1 leads to the travel time by PR effect [29]:

$$t = (a_0^2 - a_e^2)\frac{\rho r}{2k} \tag{3.2}$$

a_e is the distance at the end of the integration, for example $1AU$ at Earth's orbit. The production rate P_i of long lived nuclei i is given by [29]:

$$P_i = \sum_j \int \frac{d\Phi(E)}{dE} \times N_j \times \sigma(j \to i, E)dE \tag{3.3}$$

Where $\Phi(E)$ is the flux of incident particles as function of energy. N_j is the number of target atoms (Fe or Ni). $\sigma(j \to i, E)$ is the cross section of the target as function of the incident particle's energy. If only a set of cross sections at given energies are known, Eq. 3.3 can be approximated by [29]:

$$P_i \approx \sum_j \sum_k \frac{d\Phi(E_k)}{dE} \times N_j \times \sigma(j \to i, E_k) \tag{3.4}$$

Measurements of the proton cross sections show that most ^{53}Mn is produced by protons with an energy range from 17 to $1100 MeV$. A list with measured cross sections of ^{nat}Fe(p,x)^{53}Mn and ^{nat}Ni(p,x)^{53}Mn for proton energies from 17 to $2600 MeV$ is given by Merchel et al. [23]. Comparing the amount of ^{nat}Fe and ^{nat}Ni in ordinary chondrites (Tab.3.1) and taking into account that their cross sections are in the same order of magnitude [23], one can conclude that most of the ^{53}Mn produced

comes from the spallation on Iron ($> 90\%$) [29].

The Bateman equation describes the production of a generic radionuclide due to the irradiation of the IDPs, with a negative term accounting for the decay and two positive ones for the production by GCRs and SCRs, P_G and P_S [29]:

$$\frac{1}{m_{sample}} \frac{dN(t)}{dt} = -\frac{\lambda}{m_{sample}} N(t) + P_G(t) + P_S(t) \tag{3.5}$$

The first term on the right side accounts for the radioactive decay. $N(t)$ is the number of atoms of the radioactive isotope of interest, λ its decay constant and m_{sample} the mass of the sample. Our sample mass is that of the IDPs with their mass distribution as shown in Fig.2.3 [1] and a mean density of $\rho = 2.0 \frac{g}{cm^3}$ [30].

The proton energy spectrum in the range of the relevant cross sections for producing ^{53}Mn is not well known. Therefore the results of measurements of ^{53}Mn in lunar rocks [31] in comparison with ^{53}Mn in the Gebel Kamil iron meteorite are used [32]. Saturation is achieved when the radiation time exceeds several half life times. This was found to be the case on the Moon and the Gebel Kamil iron meteorite. A saturation activity of around $462 dpm/(kg)$ for ^{53}Mn was found on the surface of lunar samples [31]. A model used for calculating the surface value of the activity of the Gebel Kamil meteorite determined the surface activity of ^{53}Mn on the meteorite to around $350 dpm/(kg)$ [33]. Since IDPs have small radii ($\sim 10^{-5} m$) and low masses ($\sim \mu g$) using the surface values is justified. This value does include SCRs and GCRs. So the production rate of both is combined to $P_0 = P_G(t) + P_S(t)$ with P_0 being the production rate at $1 AU$. For comparison the theoretical activity of ^{53}Mn calculated by Trappitsch et al. [34] for IDPs traveling from the MB to Earth in the size range as shown in Fig. 2.3 is $P_0 = 884 dpm/(kg)$. For the calculations done in this thesis, the lowest value presented by Ammon et al. [33] on the basis on measurements published by Ott et al. [32] to estimate a lower limit is used.

Reference	Sample	depth [cm]	Iron content	$\frac{^{53}Mn\ dpm}{kg\ Fe}$ at surface
Fimiani et al. 2016	12021,14 (lunar)	0.2 ± 0.2	12.5%	535
	150008,1050 (lunar)	0.25 ± 0.25	12.6	391
			average:	462
Ott et al. 2014	Gebel Kamil	$20 - 80 cm$	78.2%	350
Trappitsch et al. 2012	Modeling for IDPs		22.5%	3929

Table 3.2: Saturation values for ^{53}Mn from Fimiani et al. [31], Ott et al. [32] and Trappitsch et al. [34] for the production rate of GCRs and SCRs. For the Gebel Kamil meteorite a model was used to calculate the surface value [33]. The surface values were taken, since IDPs have such small radii, hence their depth can be neglected. The model by Trappitsch takes into account the mass distribution as proposed by Plane [1]. The values for the Iron content for the Ott and the Fimiani value were taken from Fimiani et al. [31]. For the Trappitsch value the composition as proposed in Tab. 3.1 is assumed.

The values for the saturation activity of ^{53}Mn given in Tab. 3.2 vary by a factor of 10. For the lunar as, as well as for asteroid sample, due to the size, a 2π irradiation is assumed. There is no shielding effect for an IDP and therefore a 4π irradiation is assumed. This explains the difference by a factor of 2. On the surface of the moon the Gardening Effect constantly revolves the lunar surface [31]. So samples recovered from the lunar surface may have been shielded to the irradiation and just recently been transported to the surface. This explains the variation for the lunar sample values to the calculated value by Trppitsch to some degree. For the asteroid Gebel Kamil the uncertainties in the preatmospheric size as well as its geometry may effect the saturation value.

The saturation values by Fimiani and Ott are therefore a lower limit to the estimate the production of ^{53}Mn.

In saturation, production equals disintegration:

$$P_{^{53}\text{Mn}}(t) = N^{sat}_{^{53}\text{Mn}}(t) \tag{3.6}$$

Thus, by using the activity

$$A(t) = \frac{dN(t)}{dt} = \frac{d}{dt}N_0 e^{-\lambda t} = -\lambda N_0 e^{-\lambda t} \text{ with } \lambda = \frac{ln(2)}{t_{1/2}}$$

the initial conditions

$$A(0) = 0 \Rightarrow P_0 m_{sample} = \lambda N_0$$

$$\lim_{t \to \infty} A(t) = P_0 m_{sample}$$

and demanding P_0 to be constant, equation 3.5 becomes:

$$A(t) = P_0 m_{sample}(1 - e^{-\lambda t}) \tag{3.7}$$

The production rate P_0 is dominated by the SCR production rate for low distances from the Sun [34]. Assuming that irradiation takes place between Jupiter ($5AU$) and Earth ($1AU$), the production by GCRs will be neglected. Therefore $P_0(t)$ is proportional to $P_0(1AU/a(t))^2$ with $a(t)$ being the orbital distance with respect to the Poynting Robertson effect [29]. For simplification P_0 is set to different values representing different distances from the Sun (see equation 3.2). The results of this model are shown in Table 3.3.

$P_0 = 449[^{53}\text{Mn } (dpm/kgFe)]$ at $1AU$				
t irradiation $[10^6a]$	$A[\frac{dpm}{kgFe}]$	At.(^{53}Mn) / $(kgFe)$	At.(^{53}Mn) /m^2a	At.(^{53}Mn) in 500L
4.4	252	7.1×10^{14}	4.0×10^6	3.2×10^7
1.0	77	2.2×10^{14}	1.2×10^6	8.2×10^6
0.25	21	5.8×10^{13}	3.2×10^5	2.2×10^6
$P_0 = 50[^{53}\text{Mn } (dpm/kgFe)]$ at $3AU$				
t irradiation $[10^6a]$	$A[\frac{dpm}{kgFe}]$	At.(^{53}Mn)/ $(kgFe)$	At.(^{53}Mn)/m^2a	At.(^{53}Mn) in 500L
4.4	28	7.9×10^{13}	4.4×10^5	3.5×10^6
1.0	9	2.4×10^{13}	1.3×10^5	9.1×10^5
0.25	2	$6.4 times 10^{12}$	3.6×10^4	2.5×10^5
$P_0 = 18[^{53}\text{Mn } (dpm/kgFe)]$ at $5AU$				
t irradiation $[10^6a]$	$A[\frac{dpm}{kgFe}]$	At.(^{53}Mn)/ $(kgFe)$	At.(^{53}Mn)/m^2a	At.(^{53}Mn) in 500L
4.4	10	2.8×10^{13}	1.6×10^5	1.3×10^6
1.0	3	8.6×10^{12}	4.8×10^4	3.3×10^5
0.25	1	2.3×10^{12}	1.3×10^4	8.8×10^4

Table 3.3: P_0 is the production rate of ^{53}Mn at different distances from the Sun. The value $P_0 = 449$ ^{53}Mn$(dpm/kgFe)$ is derived from $P_0 = 350$ ^{53}Mn(dpm/kg) by converting from kg to kg Fe. The irradiation or exposure time is the PR lifetime of the average IDP being moved from different starting points (Jupiter resonance at $5AU$ with $t = 4.4 \times 10^6a$, particle set free at $3AU$ with $t = 1.0 \times 10^6a$ and the mean lifetime of cometary dust grains without interaction 0.25×10^6a[25]. A is the activity due to irradiation time and production rate. The last three columns show the calculated number of ^{53}Mn atoms per kg Fe, the accreation of ^{53}Mn atoms per year and square meter (see Chapter 4.2) and the number of ^{53}Mn atoms in antarctic snow sample collected.

Due to the lack of information concerning the lifetime of dust particles of cometary origin and not considering the mass distribution of IDPs but only an average particle mass, the results given are only a crude estimate to check, whether we are able to detect the long lived radioisotope ^{53}Mn in the antarctic snow sample. The results of the model are in agreement with other values found in literature as for example 5.5×10^7 atoms of ^{53}Mn/m^2a [35].
Comparing the results with the amount of sample material collected (Chapter 5.1), the deposition rate suggested by Plane et al. [36] (Section 4.2) and the so far achieved sensitivity by AMS concerning ^{53}Mn (Section 5.5) a measurement of interplanetary produces Manganese should be possible. The expected ratio of ^{53}Mn to ^{55}Mn is in the 10^{-14} range.

Chapter 4

Interplanetary Dust Particles in Earths Atmosphere

Earth is subjected to a constant flux of Interplanetary Dust Particles. The IDPs rain down all around the planet interacting with our atmosphere (ablating, vaporizing, condensing). A simple model of the atmosphere describes the global air flow in the mesosphere the following way: While warm air rises at the summer pole (pole where the meteorological summer is ongoing), the air at the winter pole (meteorological winter) is cooled down and drops towards the ground [37]. This creates an air stream from the summer to the winter pole, changing every six months. So supposedly IDPs entering the atmosphere and being subjected to this air stream, are deposited at the poles in a more enhanced way.

4.1 Heating, Ablation and Condensation of Interplanetary Dust Particles

While entering Earth's atmosphere IDPs are subjected to atomic sputtering by inelastic collisions with air molecules and heating due to friction. The non thermal sputtering accounts for $\sim 35\%$ of the particles mass loss for the smallest ($10^{-17} - 10^{-13}g$) and fastest ($\sim 60 - 70\frac{km}{s}$) meteoroids [30]. After reaching Earth's surface, a meteoroid becomes a meteorite. IDPs in this range only make a minor contribution to the overall mass input [1], thus non thermal sputtering only makes a minor contribution.

Heating due to friction leads to melting, boiling and evaporation leaving meteoric smoke particles (MSPs) in the upper atmosphere between 70 and $120km$ [38]. This process is influenced by several relatively unknown and uncertain parameters: The mean velocity and velocity distribution of the IDPs, the mass distribution, the density, the geometrical shape and the angle of impact. The mean velocity is $14\frac{km}{s}$ and the angle or impact $37°$ [38][30]. Both the velocity and angular distribution are shown in Fig4.1. The mean density is $\rho = 2\frac{g}{cm^3}$ [30]. For the incoming material

a spherical geometry and an ordinary chondritic composition is assumed (mostly olivine, $FeMgSiO_4$). The thermal energy that a meteoroid receives is a combination of radiative loss, temperature increase by friction, melting, phase transitions and vaporization of its constituents. This leads to the following formula [39]:

$$\frac{1}{2}\pi R^2 \rho_a v^3 \Lambda = 4\pi R^2 \sigma \epsilon (T_s^4 - T_a^4) + \frac{4}{3}\pi R^3 \rho_m C \frac{dT_m}{dt} + L\frac{dm}{dt} \qquad (4.1)$$

The left side of the equation represents the frictional heating term, with Λ being the dimensionless heat transfer coefficient, describing the fraction of kinetic energy which is transferred to the particle. ρ_a is atmospheric density, v the meteors velocity and R its radius. The first term of the right side describes radiative loss with σ being the Boltzmann constant, ϵ the emissivity (the material's effectiveness in emitting energy as thermal radiation) of the meteoroid, T_s its surface temperature and T_a atmosphere temperature. $4\pi R^2$ is the meteoroids surface. The second part considers the energy loss due to the heat capacity (phase transition and heating). With ρ_m being the meteoroids density, C its specific heat (amount of energy needed to raise $1kg$ of the bodies temperature by $1K$), T_m the mean temperature of the particle and t the time. The third and last term accounts for the heat loss due to the transfer of particle mass into the gas state. L is the latent heat of vaporization or sublimation (if the particle has not melted) and m the mass of the meteoroid.
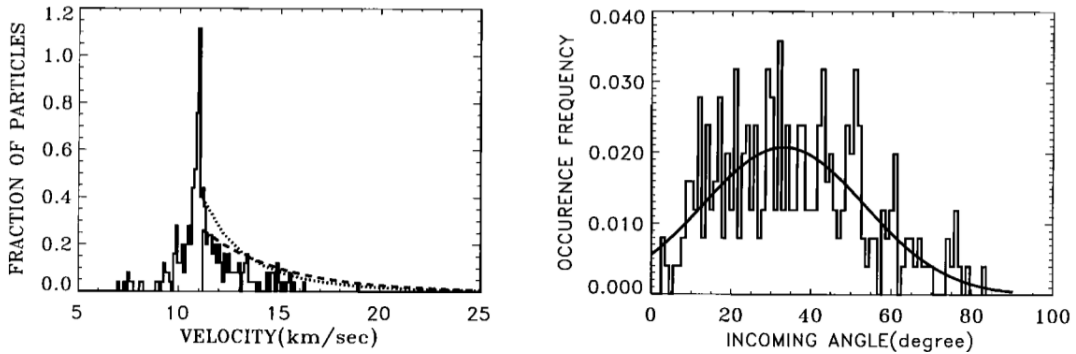

Figure 4.1: The velocity distribution (left side): empirical data (solid line) and two different fits, exponential (dashed line) and power law (dotted line). The right side shows the incoming angle distribution fitted with a Gaussian shape centered at 35°. [38]

A qualitative look at equation 4.1 shows that for small particles ($< 10^{-12}g$ or $R < 0.5\mu m$) the heat capacity term is smaller than the radiative loss term. This means that those meteoroids will not become hot enough to ablate. Particles with a mass of $> 10^{-7}g$ or $R > 23\mu m$ reach the ablation temperature [30]. The meteoroids with masses and radii in between need to encounter Earth's atmosphere with $v > 40\frac{km}{s}$ to reach $1800K$ or more. This is the temperature required for more

volatile elements like Na to evaporate [1]. The assumption is made that the incoming material loses most of its mass, up to 90% [30][40].

Since the different elements have different melting and boiling temperatures (Tab.4.1) they ablate at different altitudes (Fig.4.2). Elements with a low boiling temperature ablate at higher altitudes than those with higher boiling temperatures.

Element	K	Na	Mg	Ca	Mn	Si	Fe
$T_{melt}[C°]$	64	98	639	839	1245	1410	1535
$T_{boil}[C°]$	744	883	1090	1484	1962	2335	2750

Table 4.1: List of the most abundant elements in meteoroids (K, Na, Mg, Ca, Si, Fe) with their melting and boiling temperature. T_{melt} and T_{boil} of Manganese are added for comparison [41]. It is argued that Mn shows a similar behavior in ablation as Fe, Si and Ca because of its melting and boiling temperature being similar.
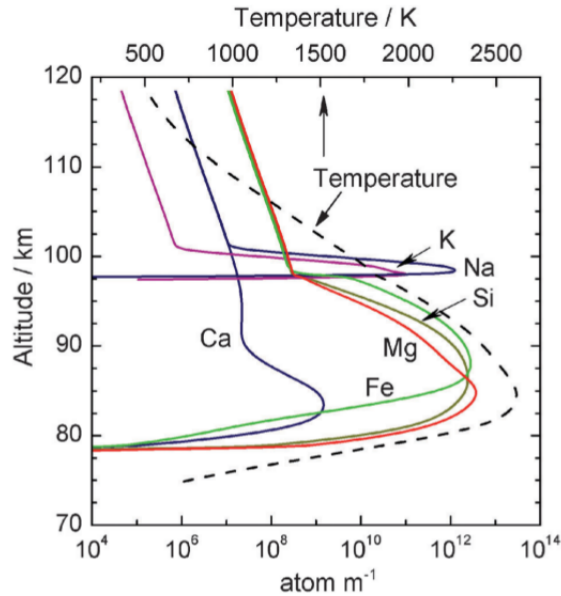

Figure 4.2: Elemental ablation profile of a $5\mu g$ meteoroid with an entrance velocity of $20\frac{km}{s}$ as predicted by the Chemical Ablation Model (CABMOD) [1]. The particle temperature is shown by the black dashed line. It is assumed that Mn ablates in the same altitude as Ca,Fe and Mg. The behavior of Mn is assumed to be similar to that of Fe in the atmosphere.

This process is described by the Chemical Ablation Model (CABMOD) [30], which includes the ablation by sputtering via inelastic collisions with air molecules before melting, diffusion of the volatile constituents of the particle (Na and K), evaporation of the atoms and oxides from the molten meteoroids, and impact ionization of the

ablated fragment by collisions with air molecules.

The velocity loss of a particle is described by [30] as:

$$\frac{dv}{dt} = -\Gamma v^2 \frac{3\rho_a}{4\rho_m R} + \rho_m g \tag{4.2}$$

with all the parameters being the same as in equation 4.1. Γ is the dimensionless free-molecular drag coefficient, describing the momentum transfer between the air molecules and the particle. Its magnitude lies between 0.5 and 1 [42]. The last term describes the gravitational acceleration and can be neglected on the basis of the velocity distribution of meteoroids ($v_{mean} = 14 \frac{km}{s}$).

For calculating the mass loss rate Langmuir evaporation is used, since it describes the evaporation of a molten liquid [43] [44]. The mass loss rate of a species i is given by [30].

$$\frac{dm_i^A}{dt} = \gamma p_i S \sqrt{\frac{\mu_i}{2\pi k_B T}} \tag{4.3}$$

The superscript A refers to thermal ablation. γ describes the probability of a molecule to stick to the surface S or to stay within the particle after a collision. p_i is the thermodynamic equillibrium pressure of a species in the gas phase and μ_i the molecular weight. T is the temperature and k_B the Boltzmann constant. The overall mass loss for ablation is given by the sum over all gas phase components [30]:

$$\frac{dm^A}{dt} = \Sigma_i \frac{m_i^A}{dt} \tag{4.4}$$

The ablated mass released consists at first of atoms and molecules. These either condensate, coagulate or react with other molecules or atoms in the atmosphere (see Fig. 4.3) to $0.2 - 40 nm$ sized meteoric smoke particles (MSPs) [37]. Running the smoke creating processes with different variables (bulk density, entrance speed etc.) shows that the ablation distribution stays qualitatively the same [37].

Comparing T_{melt} and T_{boil} for Manganese to those of Iron, Silicon and Calcium suggest its ablation to be in the same altitude. The behavior of Manganese in the atmosphere is assumed to be the same as that of Iron's.

4.2 Distribution of Interplanetary Dust and Meteoric Smoke Particles in the Atmosphere

For simplification the assumption is made, that the smoke particles in the mesosphere are evenly distributed. The residence time of the MSPs is in the range of 4 years [36]. Transportation of the particles in the mesosphere at 80 to $120 km$ follows a seasonal pattern, always transporting them to the winter pole. This is due to warm air rising at the summer pole and cold air sinking down at the winter pole. This creates a seasonal pattern changing every six months, as the Sun wanders from the northern to southern hemisphere bringing winter to the North and summer to the
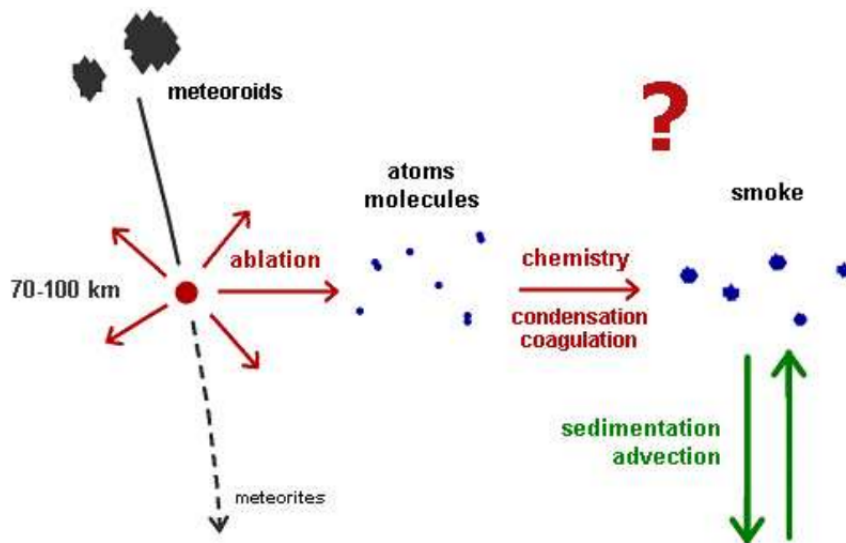
Figure 4.3: Schematic representation of a meteoroid entering Earth's atmosphere [37]. The meteoroids enter Earth's atmosphere and ablate. Meteoroids surviving this process become meteorites and fall to the ground. The ablated molecules and elements now condensate and coagulate to smoke particles. The meteoric smoke particles are now transported by an air stream and can deposit.

South. At the winter pole, MSPs are rapidly drawn downward by the polar vortex [45], a low pressure zone near the pole reaching up in the stratosphere. This leads to an enhancement of a factor of up to 6 for the dry deposition rate during the winter months [37]. After leaving the mesosphere, wet deposition becomes more important, since ice core samples from Greenland, where precipitation is seven times higher, show more MSPs than comparable samples taken in the Antarctica [46]. The Figure 4.4 shows the global deposition of Fe ablated from IDPs in the Atmosphere. Using this deposition rate and the calculated amount of ^{53}Mn compared to Iron in ordinary chondritic material allows an estimate of the deposition rate of extraterrestrial ^{53}Mn and therefore the overall IDP accretion rate by Earth.
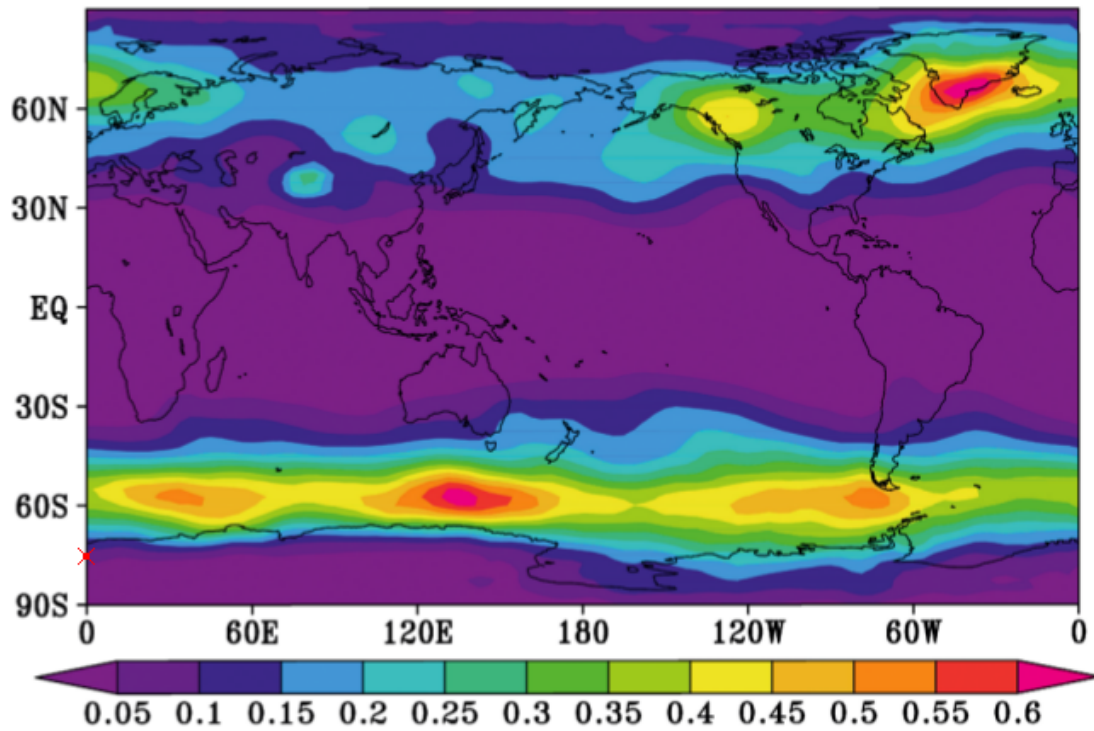
Figure 4.4: Global deposition of Fe in $\frac{\mu mol}{m^2 a}$ from mesospheric MSPs simulated for an mass input of $27 t/d$ [36]. The y-axis shows the degree of latitude, the x-axis the degree of longitude with the outlines of the world map shown for comparison in the graph. The deposition rate is enhanced at 60° North and South (in Greenland or near the Arctic) due to mesosphereric transport to the poles. Kohnen station (75°S/0°E), where the sample was recovered, is marked by a red x.

Chapter 5

Measurement of Manganese-53 in Antarctic Snow Samples

5.1 Sample Origin at Kohnen Station in Antarctica

Figure 5.1: Loaction of Kohnen station in the Antarctica [47].

At the Kohnen station in the Antarctica (75°S/0°E, $2892m$ above sea level [2]) $500L$ of snow, the equivalent of $0.5m^3$ water, were collected over a range of three years. The precipitation rate at Kohnen station is $62mm$ water equivalent per year [2]. This secluded place was chosen for sample collection, since the input of atmospheric and natural dust is very little in the Antarctica. This is due to the remoteness to civilization and industry. The low temperatures keep the sample material preserved due to low evaporation rates.

After collection the snow was transported in styrofoam boxes(for insulation) by plane to the shore of the Antarctica. From there it was sent by ship to Cape Town and from there to Bremerhaven, also by ship. From Bremerhaven the sample material was sent to Technical University Munich in Garching by truck. In Garching it was melted, filtered and filled in plastic canisters. It is important for the material to arrive in a frozen state, since basic environment in the water would have lead to a precipitation of oxides in the transport containment. To avoid this, and for conservation, the molten sample was acidulated with HNO_3. The filters were sent to the Helmholtz-Zentrum Dresden-Rossendorf for processing. The water was sent to the Technical University Vienna for evaporation and chemical treatment.

5.2   Filtering of the molten Snow

Before chemically processing the molten antarctic snow, the water was filtered with two different filters ($12 - 15\mu m$ and $2 - 3\mu m$). Around 205 MMs were collected of the filters. The combined mass of those MMs is around $0.25mg$ [1]. The filters were sent to Dresden at the Helmholtz-Zentrum Dresden-Rossendorf and are processed as proposed in Merchel et at. [5] to extract Manganese.

5.3   Chemical Treatment of the Sample

The sample preparation for the remaining IDP traces in the water was done at the Atom Institute at the Technical University of Vienna. Experiments to achieve a better Chromium suppression for smaller sample material and minimize the usage of acids were performed there. It is important to achieve the best possible chemical suppression of Cr, since the isobaric ^{53}Cr behaves so similarly in the beam line and the GAMS to ^{53}Mn that it is difficult to separate those isobars with AMS techniques. This means that a good chemical separation is necessary to achieve the sensitivities needed to detect ^{53}Mn in antarctic snow. Acids have a non-negligible contamination of different metals in regard to AMS measurements. This means that an excessive use of acids can lead to a higher isobaric background. The improvement of the separation was done on the basis of the work by Merchel et al. [5].

Measurements with X-ray fluorescence spectroscopy (TXRF) and inductively coupled plasma mass spectronomy (ICP-MS) of the molten and evaporated snow showed

---

[1]Email form Andreas Gärtner, Senckenberg Gesellschaft für Naturforschung, 12th of may 2017

that the $500L$ contained $150\mu g$ Mn, $400\mu g$ Fe, $200\mu g$ Ni, $50\mu g$ Cr [2] . Dummy samples with about the same elemental ratio were made from different standard material (Iron Standard, 1000 $\mu g/mL$, Ultra Science; Nickel Standard, 1000 $\mu g/mL$, Ultra Science; Manganese Standard, 1000 $\mu g/mL$, Ultra Science; Chromium Standard, 1000 $\mu g/mL$, Ultra Science). These dummies were subjected to the chemistry suggested by Merchel et al. [5], with the difference that smaller columns and less acid is used. The materials used are a Dowex Ion exchanger, 1X8, 200-400 mesh, Serva Feinbiochemie, p.a., and a Tristkem AC-141-AC columns (2 mL).

For the preparation of the column, a slurry of Dowex in $10mol/l$ HCl is filled into it. The excess of the HCl is drained. The column is washed with $10mol/l$ HCl until the eluate is clear. The column was conditioned with $6mol/l$ HCl.

For the dummy $5mL$ Fe standard, $200\mu L$ Ni standard, $150\mu L$ Mn standard and $50\mu L$ Cr standard are mixed and evaporated to complete dryness on a heating plate ($200°C$). The dried sample was dissolved in $400\mu L$ of $6mol/l$ HCl.
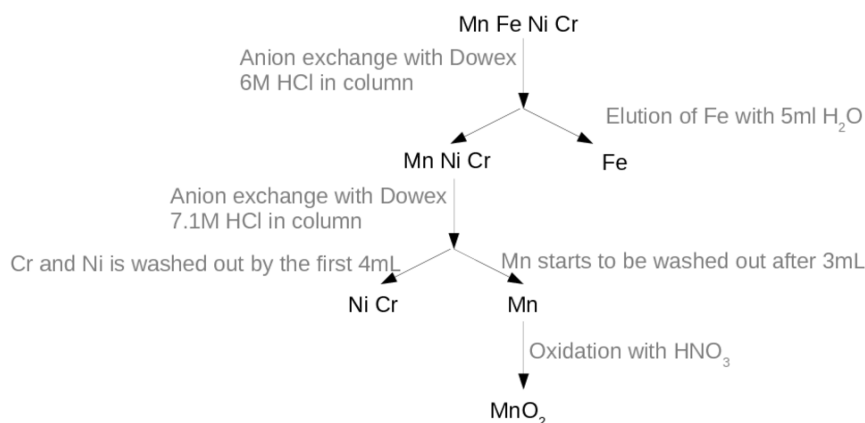

Figure 5.2: Scheme for the Manganese separation as described in the text. M stands for molar $[mol/L]$. Different M of HCl are used for the different elements to separate in the column filled with Dowex resin. For the Mn separation the amount of acid added is important, since Cr is dissolved by fewer fractions of acid than Mn. For a Mn-Cr-separation profile with respect to fractions of HCl added see Fig. 5.3.

The liquid standard dummy was pipetted on the frit, covering the column to prevent it from going dry. The Cr, Mn and Ni were eluted with $5mL$ $6mol/l$ HCl. This leaves the Iron on the Dowex column. Iron can be eluted by adding another $5mL$ H_2O. The remaining standard material with Cr, Mn and Ni in it, was again eluted in HCl. Afterwards the eluted standard was pipetted in another column filled with Dowex ion exchange resin, to trap the Mn and the Cr. The Cr and Mn separation was done by giving $7.1mol/l$ HCl in the column. Cr needs less HCl than Mn to be washed out of the Dowex resin. Adding the right amount of acid washes the Cr out

_____

[2]Personal contact with Jan Welch, Technical Universality of Vienna

of the column leaving the Mn behind. This Mn is then extracted by adding more HCl. After the extraction of Mn from the Dowex, it was dried and then oxidized by adding NHO_3 [48]. In the separation scheme by Merchel et al. [5] the oxidation is done by heating the extracted Mn up to $800°$.
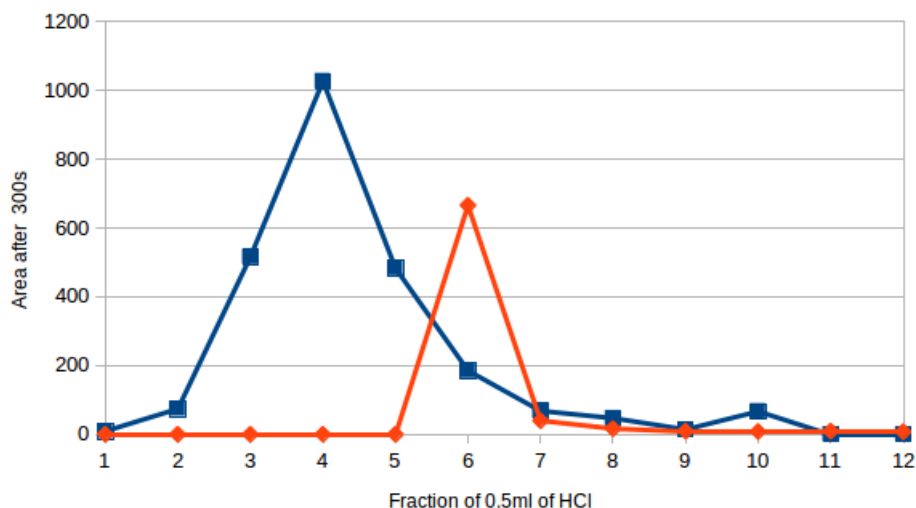

Figure 5.3: Separation profile of Manganese (orange) and Chromium (blue) with, data taken form [48]. ^{54}Mn ($t_{1/2} = 312d$) and ^{51}Cr ($t_{1/2} = 28d$) are added to the dummies as tracers. After adding steps of $0.5mL$ HCl to the column the fractions are analyzed by γ-spectroscopy. After adding a certain amount of HCl ($\sim 5.5mL$) most of the Cr is eluted off the column and Mn starts to wash out. The width and height of the peaks in the spectrum depend on the concentration of the acid. By being of in the concentration the separation point changes.

By preparing a sample with radioactive ^{51}Cr ($t_{1/2} = 28d$) and ^{54}Mn ($t_{1/2} = 312d$) made at the TRIGA Mark-II reactor at ATI Wien as tracers, the separation behavior of Mn and Cr was determined (Fig. 5.3). Fractions of HCl ($1mL$) were given through the column and the eluted material is measured by γ-spectroscopy for its Cr and Mn content. It was found that the separation is very sensitive to the concentration of the acid and therefore to the amount of acid added, since the separation point of Cr and Mn changes. This means that small changes in the concentration of the acid and so the amount needed have a big influence on the suppression of the Cr background. After the tests performed at the TU Vienna, the dummies were sent to the TUM for measurement by AMS. Here the Cr background was determined (see Table 5.1 and Table 5.2).

Furthermore different samples were taken from different steps of the separation process, to determine which steps add Chromium. Looking at Table 5.1, the effect of the oxidation with HNO_3 due to adding Cr can be seen. Also shown are the results

of giving the standard material through two or three columns before oxidation is shown. The background can be suppressed by a factor of 100 by a third column. But by using more column's sample material is lost. So the usage of more columns is limited for small sample size.

In table 5.2 the sole contribution of one column to the Cr background is shown to be zero (see Sample SF027). Looking at SF026 in Table 5.2 the oxidation from Mn to MnO_2 by HNO_3 adds a factor of around 100 to the Cr background. To see whether the Manganese of the TU Munich behaves different in separation than the TU Vienna's due to Cr separation (SF028 and SF925 in Table 5.2). This attend fail due to an error in the sample preparation.

Name	Material and process	^{53}Cr event rate $[Hz]$	$\frac{Event\ rate}{Blank\ rate}$
Blank	MnO_2 (MUC) with Ag powder in Ag holder	0.03	1
1	Mn (VIE) one column, oxidized with HNO_3	8	267
2	Mn (VIE) + Cr two columns	158	5267
3	Mn (VIE) + Cr three columns	27	900

Table 5.1: Chromium events from different sample dummies in comparison to a blank. The ^{53}Cr events counted are normalized to the events of the blank material. The error is around 20%. The addition MUC and VIE shows whether Manganese used is from the TUM or the TUV. A comparison of the different Mn samples is done to exclude impurities in one of them (see Table below). The blank consists of Mn mixed with pure Ag powder. Sample 1 is a Mn standard without additional Cr separated in a column with a following oxidation by HNO_3. Samples 2 and 3 were made of Mn and Cr standard material and given through two and three columns.

Name	Material and process	^{53}Cr event rate $[Hz]$	$\frac{Event\ rate}{Blank\ rate}$
Blank	MnO_2 (MUC) with Ag powder in Ag holder	333	1
SF027	Mn (MUC) one column	330	1
SF026	Mn (MUC) oxidized with HNO_3	26336	88
SF028	Mn (MUC) + Cr two columns	214100	717
SF025	Mn (VIE) + Cr two columns	20300	67

Table 5.2: Chromium events from different sample dummies in comparison to a blank material, with Manganese from the TUM (MUC) and the TUV (VIE). The ^{53}Cr events counted are normalized to the events of the blank material. The error is around 20%. SF027 was Mn from the TUM treated with one column to see whether the column contributes to the Cr background. SF026 was Mn from the TUM oxidized with HNO_3 five times. SF028 and SF027 are two standards made from the Mn from the TUM and from the TUV, to see whether the used Mn has an effect on the separation. The results show, that no Cr was added by preparing the sample SF025.

Conclusion: For the snow sample, the separation will be done with two columns. The sample mass loss for one column is between 10 and 15% [3]. Using a third column would withdraw too much sample mass. For the separation to be done well, practice by the performing chemist will be needed with radio tracers to hit the separation point. The oxidation will be done by heating the sample up to $800°C$ instead of adding HNO_3.

---

[3] Personal contact with Jan Welch, Technical Universality of Vienna

5.4 Accelerator Mass Spectrometry at the Maier-Leibnitz-Laboratory in Garching

Accelerator Mass Spectronomy (AMS) is based on the deflection of charged particles moving in a magnetic field. The Lorentz force drives these ions into circular trajectories with different radii for different masses and/or energies.
This simple principle is the foundation in great achievements for the understanding of nature by AMS world wide.

At the Maier-Leibnitz-Laboratory (MLL) in Garching, a high voltage tandem accelerator (up to $14MV$) in combination with a gas-filled analyzing magnet system (GAMS) is used to perform AMS. The combination of high energies of the measured isotopes through the high voltage acceleration and the GAMS enables to reach sensitivities of up to 10^{-16} of long lived radioactive nuclei to their stable counterpart. A sputter ion source is used to create negative ions. A first deflection of the negative ion beam extracted from the source is done by the injector magnet. This also provides the first mass separation. The ongoing beam is lead to the low energy part of the tandem accelerator receiving its first acceleration. After this first acceleration a carbon stripper foil changes the particle's charge to a statistically distributed multiple positive value by stripping off electrons. The foil also breaks up molecules with the same mass and charge of the extracted isotopes, leading to a separation only leaving the isotopes and its isobars. After the foil the beam goes through a second acceleration caused by the now multiply positively charged beam particles receiving the now opposite voltage difference at the high energy part, resulting in a multiple acceleration. In the next step an analyzing magnet is used to select a specific energy to charge ratio. The beam is then led to the GAMS for detection (Fig.5.4). Wien filters are used for the suppression of isobars. The whole beam transport takes place in a ultra high vacuum (up to $10^{-7}mbar$).

5.4.1 The low Energy Side: The Ion Source and first Mass and Energy Separation

The source used to obtain the ion beam is a cesium sputter ion source. The sample material is pressed in a sample holder made of an ultra pure metal (Gold, Copper, Aluminum or Silver, used for manganese) to reduce contamination. The sample in most cases is a metallic oxide (e.g. MnO). Since for some oxides the thermal and electrical conductivity is not adequate, the sample oxide is mixed with an ultra pure metal as matrix (e.g. Ag-powder for MnO). This ensures an even distribution of heat and the electric charge in the sample and sample holder.
Cesium is extracted from a heated cesium container connected to the source via a little tube. The tube transports the Cs to the ionizer. The ionizer is a spherical tantalum surface, for a better focus of the Cs-beam, heated up to $1000°C$. The Cs atoms are drawn to the sample through the sputter voltage ($6kV$)to sputter

material off the sample and donate electrons. This sputtered material has a charge distribution reaching from a few positive to a single negative charge. The amount of negatively charged material is linked to the electron affinity of its ions. The higher the affinity the more negatively charged particles. Now the negative particles are accelerated backwards by the same voltage ($6kV$) and then extracted out of the source by an extraction ion voltage of $28kV$ (Fig. 5.5). The extracted ion beam's current is in the range of a few hundred nA. After the extraction a first mass separation is done by the 90° injector magnet. The following electric deflection made by a 18° deflector separates by energy.

Mn has an electron affinity of zero and does not from negative ions. So Mn is extracted via MnO^-. Unfortunately the isobaric Cr, which can be found to some degree in almost every metal, builds CrO^- with the same efficiency. So it is not possible to separate Chromium from Manganese through the accelerator alone.
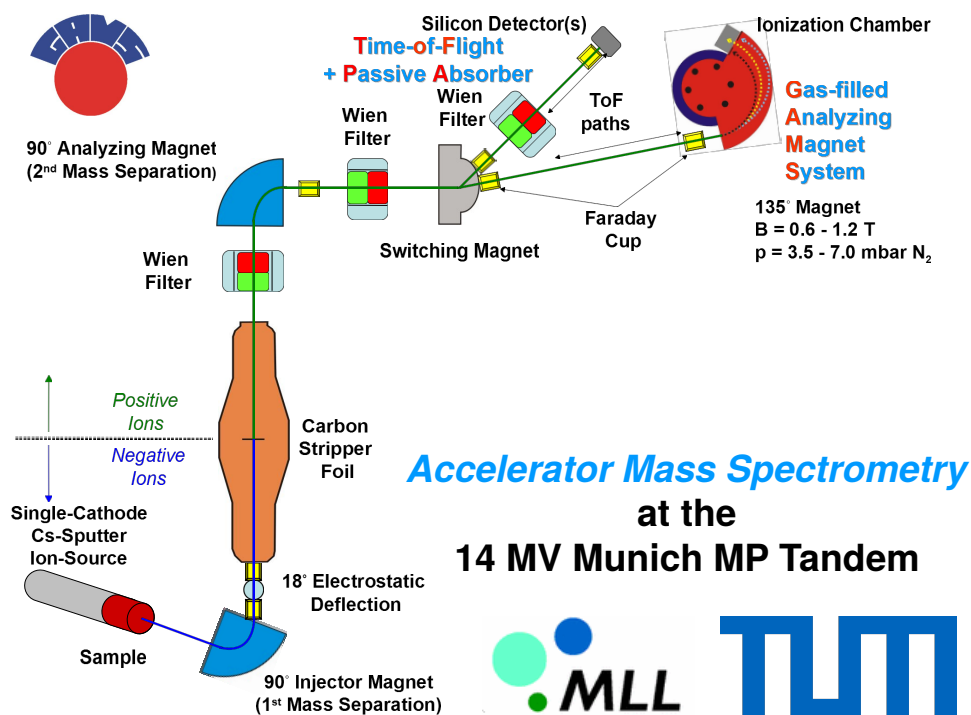
Figure 5.4: Beam transport at the MLL in Garching: Negative ions are extracted at the source. A first mass separation is done by the injector magnet. At the carbon stripper foil molecules are broken up and the beam particles receive a positive charge. After acceleration in the tandem and beam particle selection at the analyzing magnet with second mass separation. The beam is then led to the GAMS.
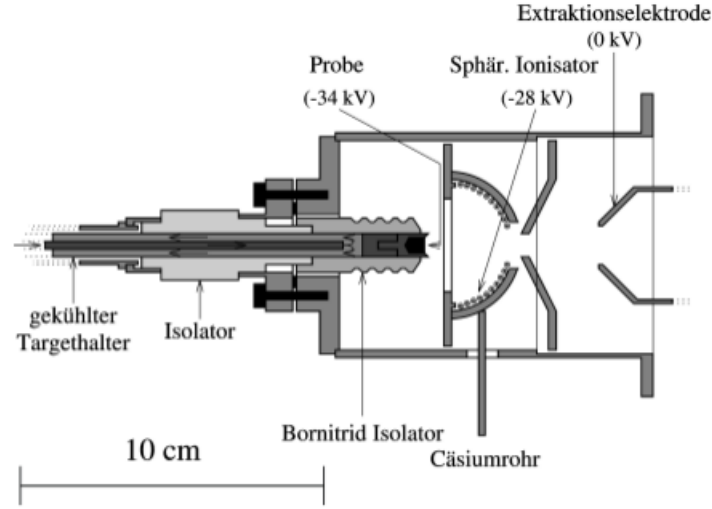
Figure 5.5: Schematic image of the ion source.

5.4.2   The Tandem

After the first mass and energy separation the beam is accelerated by a $150kV$ voltage and shot into the tandem. In the first half of the tandem an acceleration voltage of around $U = +12,700MV$ acts on the beam. Here the beam particles, the oxides from above and other molecules with the same mass and energy, increase their energy by $E = Ue$, with $e = 1$ being one atomic charge. After this the beam hits a carbon stripper foil ($\rho = 4\frac{g}{cm^2}$). This foil breaks up the molecules, to obtain a perfect molecule suppression, and charges the single atoms statistically positive by stripping of electrons. For Mn most ions are those of the $q = 10^+$ state. But since it is important to have high energies for the isobaric separation in the GAMS, the $q = 11^+$ charge state with a yield of around 20% is used.

After the foil, the ions increase their energy again by $E = Uqe$, because the acceleration voltage now acts in the opposite direction.

The energy of an ion after the tandem accelerator is then:

$$E = [U_{pre} + (\frac{A}{M} + q)U_T] \tag{5.1}$$

With U_{pre} being the preacceleration voltage of $150kV$, U_T the tandem acceleration voltage of $12.7MV$, A the atomic mass, M the mass of the molecule and q the positive charge after the stripper foil. For ^{53}Mn, the energy is in the range of $E = 150MeV$.

5.4.3 The high Energy Side: Wien Filter and Analyzing Magnet

After leaving the tandem, the beam goes though a Wien Filter (WF). The filter is used to select a specific velocity to energy ratio, since all beam particles coming from the tandem have the same energy but different velocities because of their different masses. This is done by using the Lorentz and the Electric force:

$$F_L = qv \times B = q \times E = F_{El}$$

The mass difference between ^{53}Mn and ^{53}Cr is about 0.01%. This mass difference is too small for the WF to separate.

Next in line is the 90° Analyzing Magnet (AM). The magnet is tuned to the magnetic rigidity $B\rho$ for a mass of 53, a electric charge of $q = 11$ and a terminal voltage of $12, 7MV$:

$$B\rho = \frac{\gamma m v}{q}$$

With B being the magnetic field, ρ the radius of the trajectory, γ the Lorentz factor ($\gamma \approx 1$ for $E \approx 150MeV$), m the mass, v the velocity and q the charge. Tuning the beam to the GAMS for detection is done by using a stable ^{55}Mn-beam. For this beam to be able to pass the AM the terminal voltage is adjusted since B, ρ, m and q are restrained. Just like the WF the AM is not able to separate ^{53}Cr from ^{53}Mn due to the small mass difference.

Figure 5.6: Chart of nuclides with radioactive decay and nuclear reactions scheme. ^{53}Mn and its isobar ^{53}Cr are highlighted.

5.4.4 The Gas-filled Analyzing Magnet System

The GAMS consists of a $16t$ $135°$ dipole magnet with an average deflection radius of $90cm$ and a Frisch grid ionization chamber.

The magnet chamber is filled with nitrogen gas of a few *mbar* in pressure. To protect the vacuum in the beam line a $0.9\mu m$ Mylar foil separates the line from the magnet chamber. An ion going through a gas hits the gas atoms depositing energy, leaving charge or receiving charge. The average charge of an ion going through a gas receives is proportional to its proton number Z. The higher Z, the higher the average charge received in the gas and the smaller the radius of the trajectory in the magnet. Sayer [49] also describes the energy dependence of this process, meaning that high energies result in a bigger charge difference for isobars than smaller ones (Fig.5.7). For this reason it is important to have a high energy beam, but not so high that it can not be stopped in the ionization chamber. So ^{53}Mn with $Z = 25$ will have a trajectory with a smaller radius than ^{53}Cr with $Z = 24$ (Fig. 5.8 and 5.9.)
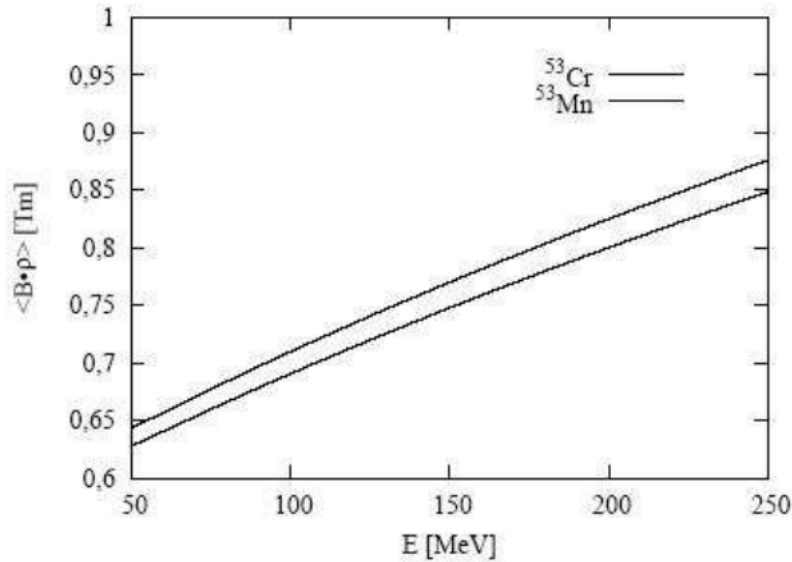
Figure 5.7: Energy dependence of the magnetic rigidity as descriebed by Sayer for ^{53}Mn (lower line) and ^{53}Cr (upper line). The difference in rigidity and so the difference of the trajectories grows for higher energies

For high values of pressures in the magnet chamber the diameter of the beam widens, since collisions with the gas atoms scatter the beam particles. Also the charging process of the ions widens the beam, because of charge state fluctuations. On the other hand the higher the pressure, the better the separation, since more collisions in the gas lead to a better statistic and therefore a smaller beam diameter with a smaller deviation of $\bar{q}$. For the energy loss measurement in the ionization chamber it is important for the beam not to lose too much energy in the magnet gas. A good compromise between these effects in the case of manganese is achieved by setting the magnet chamber gas pressure to roughly $5mbar$.
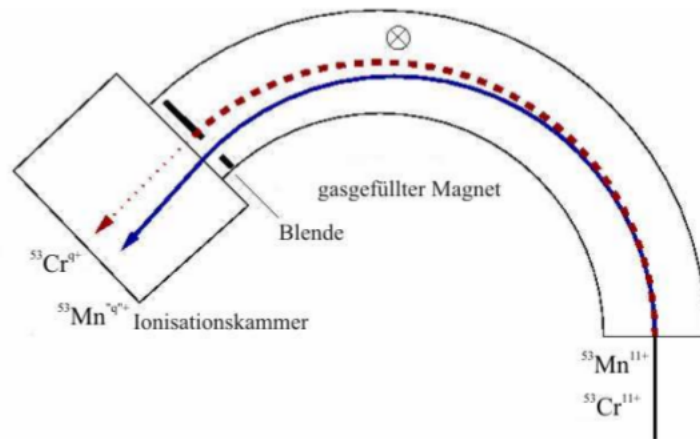
Figure 5.8: Qualitatively trajectories of the different ions in the gas magnet.

Before entering the ionization chamber, a aperture is used to suppress the now locally differing isobaric ^{53}Cr several orders of magnitude as seen in Figure 5.8. The magnet gas chamber is separated from the ionization chamber by a $2\mu m$ Mylar foil.
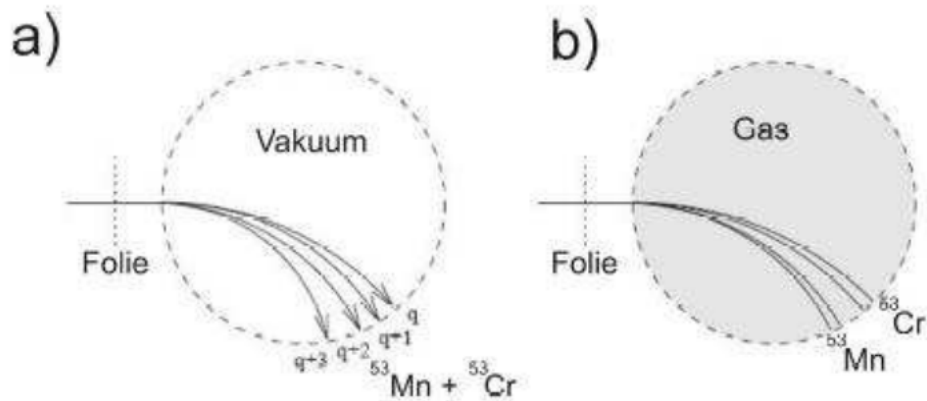

Figure 5.9: Schematic depiction of the isobar separation in a gas filled magnet with ^{53}Mn and ^{53}Cr as example. **a)** The positive charged ions are stripped by the foil while entering the vacuum and receive different charge states for isobaric ions in the same charge state. This leads to similar trajectories. With gas as seen in **b)** the collisions of the ions with the gas molecules lead to different mean charges $\bar{q}$ of the isobars with different Z and make it possible to separate them by place, since they arrive at different places.
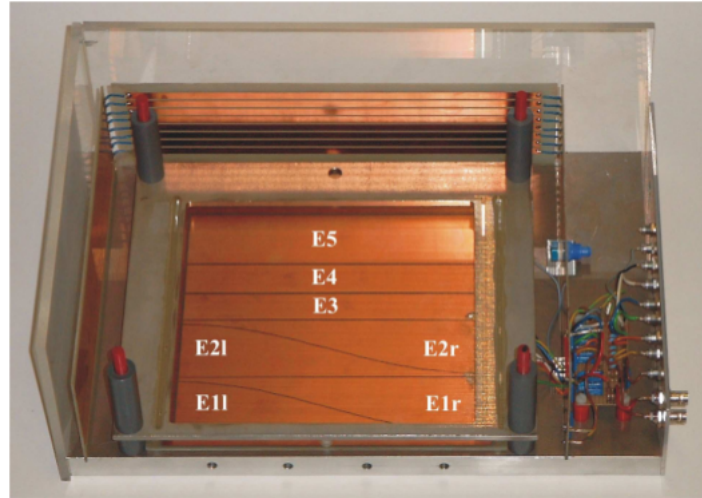
Figure 5.10: Picture of the ionization chamber with its five anodes. The first two are diagonally divided diagonally to obtain information on the position.

The Frisch gird ionization chamber filled with isobutane (C_4H_{10}) consists of five anodes with the first two anodes being divided diagonally (Fig. 5.10). The beam particles being stopped in the chamber leave free charges in the gas, positive ions an electrons, being attracted to the anodes (e^-) or cathodes (positive charges). The number of free charges, and therefore the energy deposition, depends on the energy and the Z of the stopped particle. This means that different charged particles stop at different places in the detector. So different isobars have an element specific behavior of energy deposition and come to hold at different depths in the detector. In this way it is possible to separate isobars by looking at the different anode signals and where they came to a halt [50]. The diagonal partition of the first two anodes enables to measure the position and entrance angle of the ions to dismiss scattered ones. Through the signals time difference from the first to the third anode it is also possible to determine the vertical angle of incidence.

For ^{53}Mn and the isobar ^{53}Cr a pressure of $\sim 42 mbar$ is used to stop all beam particles in the fifth anode. This is important to obtain all the energy loss information in the detector.

5.5 Measurement Routine for ^{53}Mn

The first step for a measurement is the tuning of the beam line. For this a tuning blank is used, which is made of a matrix, carrying the stable isotope of the radioactive material one wants to measure. For ^{53}Mn the stable isotope is ^{55}Mn as oxide mixed with the same weight of Ag powder as matrix. The injector magnet is set to extract the mass of 71 (^{5}Mn^{16}O) since Mn does not form negative ions but MnO does. Now the tuning blank is exchanged with a sample, a blank or standard. The

macroscopic current of this beam is measured with Faraday cups located after the injector magnet, after the tandem and in front of the GAMS to obtain the transmission. Afterwards the injector magnet field is lowered from mass 71 to 69 (^{53}Mn^{16}O). The tandem voltage is raised to keep the rigidity of the analyzing magnet fixed and the Wien filter is changed from ^{55}Mn^{11+} to ^{53}Mn^{11+}.

AMS measurements are relative measurements. This means that for the determination of the ^{53}Mn/^{55}Mn ratio of an unknown sample one with a known ratio called standard sample is needed. The standard is also used to quantify the transmission of ^{53}Mn to the GAMS. To obtain the Chromium background, a blank sample without any ^{53}Mn, but a known amount of ^{53}Cr (usually ppm range) is put in the source for a short time to prevent cross talk. The blank events make it possible to see the characteristic energy loss of the disturbing 53Cr isobar in the detector and are used to set software windows for cutting out the ^{53}Cr events in the energy signals. Now the sample of interest can be measured and the ratio of ^{53}Mn to ^{55}Mn be determined. In order to get a good statistic for the mean transmission and ^{53}Cr suppression, this procedure is repeated several times during one beam time with the measurements for the sample and blank taking up to several hours. The data is analyzed with the analyzing program MARABOU (MBS and ROOT Based Online/Offline Utility)[51].

Figure 5.11 shows spectra of the energy loss at the fourth anode for a standard (a)(^{53}Mn/^{55}Mn= 3×10^{-9}) and a blank (b) with ^{53}Cr but no ^{53}Mn, without any software windows. The first two anodes create a position signal and all anodes an energy loss signals, ΔE_1 to ΔE_5. The different regions for ^{53}Mn and ^{53}Cr are shown in (a). By comparing the spectra shown in Figure 5.11 (a) and (b), one can determine the regions of interest for ^{53}Mn in the ionization chamber by setting windows in all energy spectra. This restricts the energy and position of the ^{53}Mn signals. This way the the signals of the Chromium spiked blank, which have not been cut off by the other windows on the edge of the ^{53}Mn area, are dismissed. The spectra (c) and (d) in Figure 5.11 show the detector signals with the software windows. In the chromium spiked blank spectrum are four events in the ^{53}Mn region left (d). These are signals created by scattering of chromium on the entrance foil or other parts of the detector. It is not possible to remove those signals by setting windows, so a good chemical separation of Mn and Cr is important for the suppression of the Cr background. Chemical separation determines the background limit of ^{53}Cr. In Figure 5.11 the background was determined to be $\sim 10^{-4}$. Suppression of 6.3×10^7 for Manganese measurements have been already achieved at the MLL. A background suppression of e.g. 10^{-6} means that one signal has to be subtracted from the total amount of events, when the total amount of ^{53}Cr events is 10^6. The background also depends on the Cr suppression in the sample of interest.

For the determination of the Chromium background, sample dummies (see Chapter 5.3) are placed in the source and the terminal voltage is set to $10MV$. The current of the sample dummies and the Cr events in the detector are measured. To estimate the background rate, the events of the dummies are normalized to the Cr events of

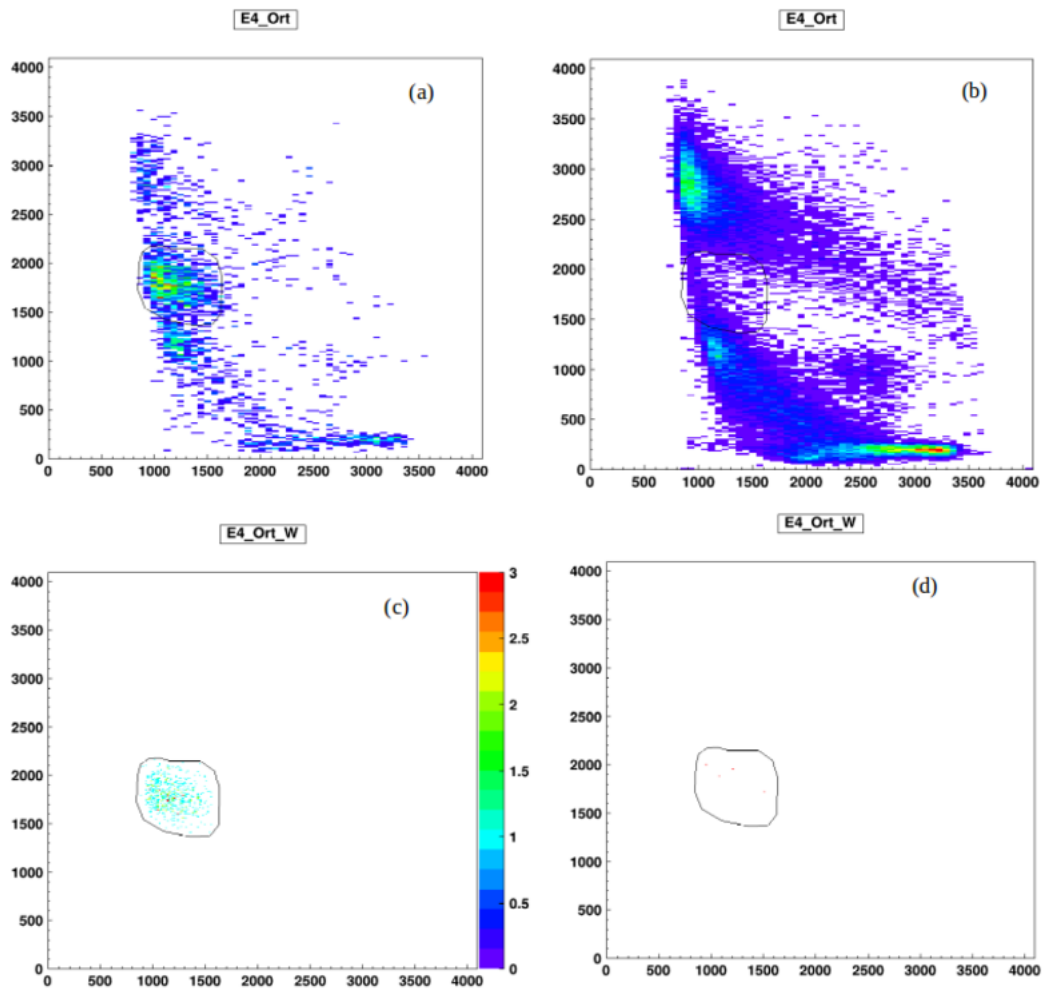a blank which is very pure in Cr.

Figure 5.11: Energy spectrum (y-axis) against the position (x-axis) in ΔE_4. (a) shows a standard sample with a ratio of $^{53}\text{Mn}/^{55}\text{Mn} = 3 \times 10^{-9}$ without software cuts for ^{53}Mn counts. (c) shows the same spectrum with cuts optimized for 53Mn signals. (b) shows a blank sample without software windows and (d) with the windows.

Chapter 6

Conclusion and Outlook

6.1 Conclusion

In Chapter 2 new results concerning the origins of IDPs were summarized, showing that around 90% of the dust grains in the ZC are of cometray origin and hence IDPs with cometary origin make up most of the Earth's mass input.

A model to estimate the irradiation of IDPs is described in Chapter 3. By working this model with different values for the production rate and different exposure times, the number of ^{53}Mn atoms expected in the antarctic snow sample was determined to be in the low 10^5 to the mid 10^7 rage.

The behavior of IDPs entering Earth's atmosphere and a model for the global deposition was shown in Chapter 4. 90% of the IDPs ablate in the mesosphere and condense to nm sized smoke particles. A model of the pattern for the global deposition of Iron from IDPs ablated in the mesosphere determines the deposition rate at Kohnen station to be $0.1 \mu mol/(m^2 a)$. Therefore one can draw conclusions for the deposition rate of ^{53}Mn being in the mid 10^7 $atoms/m^2 a$ rage or lower in combination with the model described in Chapter 3. This value is in agreement with values given in literature.

Furthermore the process of improving the chemical separation for the low amount of sample mass in the sample collected at Kohnen is shown and explained in Chapter 5. The usage of acids is reduced by working with smaller columns. The measurement method by AMS at the MLL is displayed and it is shown that the expected amount of ^{53}Mn is measurable.

6.2 Outlook

^{53}Mn almost exclusively produced by spallation of protons from cosmic rays on Iron in IDPs outside Earth's atmosphere is a tracer element for accretion of interplanetary dust on Earth. Knowing the deposition rate of this cosmogenically produced long lived radioisotope and assuming the Iron content of the IDPs will help do diminish the uncertainties of Earth's accretion rate of interplanetary dust. The limits of this approach for the determination of our planet's daily mass input are the uncertainties in modeling the ablation, transport of IDPs in the atmosphere and deposition on Earth, as well as their composition.

In this thesis it was shown that the amount of ^{53}Mn to expect in a sample collected at Kohnen station in the Antarctica is the in low 10^5 to the mid 10^7 range for the number of atoms and that a measurement of this long lived radioisotope in the snow sample by AMS at the MLL will be possible, mainly due to enhanced chemical separation of the isobaric ^{53}Cr. The suppression of ^{53}Cr in the sample by chemical treatment and in the GAMS are sufficient to measure down to the expected ratio of ^{55}Mn/^{53}Mn the 10^{-13} to 10^{-14} range.

Appendix A

List of Acronyms

AM	Analyzing Magnet
AMS	Accelerated Mass Spectrometry
CABMOD	Chemical Ablation Model
GCR	Galactic Cosmic Ray
ICP-MS	Inductively Coupled Plasma Mass Spectroscopy
IDP	Interplanetary Dust Particle
IMS	Interstellar Medium
IRAS	Infrared Astronomical Satellite
JFC	Jupiter Family Comet
KB	Kuiper Belt
MB	Main Belt
MLL	Maier Leibnitz Laboratory
MM	Micro Meteorite
MSP	Meteoric Smoke Particle
MUC	Munich
OC	Oort Cloud
PR	Poynting Robertson
SCR	Solar Cosmic Ray
TXRF	X-ray Fluorescence Spectroscopy
VIE	Vienna
WF	Wien Filter
ZC	Zodiacal Cloud
ZCM	Zodiacal Cloud Model
ZL	Zodiacal Light

List of Tables

List of Figures

Bibliography

[1] J. M. C. Plane, "Cosmic dust in earth's atmosphere," *Chemical Society Reviews*, vol. 41, pp. 6507–6518, 2012.

[2] G. Birnbaum, R. Brauner, and H. Ries, "Synoptic situations causing high precipitation rates on the antarctic plateau: observations from kohnen station, dronning maud land," *Antarctic Science*, vol. 18, no. 2, p. 279–288, 2006.

[3] M. Poutivtsev, *Extraterrestrisches ^{53}Mn in hydrogenetischen Mangankrusten*. PhD thesis, Techischne Universtiät München, Fakultät für Physik, 2007.

[4] T. J. J. C. Schätz, "^{53}Mn in extraterrestrischer Materie," Dipolmarbeit, Technische Universität München, Fakultät für Physik, 1997.

[5] S. Merchel and U. Herpers, "An update on radiochemical separation techniques for the determination of long-lived radionuclides via accelerator mass spectrometry," *Radiochimica Acta*, vol. 84, pp. 215–219, 01 1999.

[6] J. Klacka, "Poynting-Robertson effect," *Observations and Physical Properties of Small Solar System Bodies, Proceedings of the Liege International Astrophysical Colloquium 30, Liege: Universite de Liege, Institut d'Astrophysique*, p. 343, 1992.

[7] G. J. Flynn, "Interplanetary dust particles collected from the stratosphere: physikal, chemical, and mineralogical properties and implications for thier sources," *Planet. Space. Sci.*, vol. 12, pp. 1151–1161, 1994.

[8] D. Nesvory, P. Jenniskens, H. F. Levison, W. F. Bottke, D. Vokrouhlicy, and M. Gounelle, "Cometary origin of the zodiacal cloud and carbonacous micrometeroites," *The Astrophysikal Journal*, vol. 713, pp. 816–836, 2010.

[9] "Poynting Robertson effect." `http://planetfacts.org/poynting-robertson-effect/`. Accessed: 2018-13-3.

[10] "The Planets in Our Solar System." `https://pics-about-space.com/nine-planets-our-solar-system?p=3#`. Accessed: 2018-3-3.

[11] A. Morbidelli, "Origin and dynamical evolution of comets and their reservoirs," *arXiv:astro-ph/0512256*, 2005.

[12] "PIA17046: Voyager Goes Interstellar." `https://photojournal.jpl.nasa.gov/catalog/PIA17046`. Accessed: 2018-13-3.

[13] A. Moro-Martín and R. Malhotra, "Dynamical models of kuiper belt dust in the inner and outer solar system," *The Astronomical Journal*, vol. 125, no. 4, p. 2255, 2003.

[14] S. Yamamoto and T. Mukai, "Dust production by impacts of interstellar dust on edgeworth-kuiper belt objects," *Astronomy and Astrophysics*, vol. 329, pp. 785–791, 1998.

[15] J.-C. Liou, H. A. Zook, and S. F. Derm, "Kuiper belt dust grains as a source of interplanetary dust particles," *Icarus*, vol. 124, no. 2, pp. 429 – 440, 1996.

[16] S. G. Love and D. E. Brownlee, "A direct measurement of the terrestrial mass accretion rate of cosmic dust," *Science*, vol. 262, no. 5133, pp. 550–553, 1993.

[17] G. Cremonese, P. Borin, A. Lucchetti, F. Marzari, and M. Bruno, "Micrometeoroids flux on the moon," *A & A*, vol. 551, p. A27, 2013.

[18] M. A. Belyaev and R. R. Rafikov, "The dynamics of dust grains in the outer solar system," *The Astrophysical Journal*, vol. 723, no. 2, p. 1718, 2010.

[19] S. J. Kortenkamp and S. F. Dermott, "Accretion of interplanetary dust particles by the earth," *Icarus*, vol. 135, no. 2, pp. 469 – 495, 1998.

[20] H. Yang and M. Ishiguro, "Origin of interplanetary dust through optical properties of zodiacal light," *The Astrophysical Journal*, vol. 813, no. 2, p. 87, 2015.

[21] W. F. Levison, Harold F.and Bottke, G. Matthieu, M. Alessandro, N. David, and T. Kleomenis, "Contamination of the asteroid belt by primordial transneptunian objects," *Nature*, vol. 460, pp. 364–366, 2009.

[22] R. Michel, M. Lüpke, U. Herpers, R. Rösel, M. Suter, B. Dittrich-Hannen, P. Kubik, D. Filges, and P. Cloth, "Simulation and modelling of the interaction of galactic protons with stony meteoroids," *Planetary and Space Science*, vol. 43, no. 3, pp. 557 – 572, 1995.

[23] S. Merchel, T. Faestermann, U. Herpers, K. Knie, G. Korschinek, I. Leya, R. Michel, G. Rugel, and C. Wallner, "Thin- and thick-target cross sections for the production of 53mn and 60fe," *Nuclear Instruments and Methods in Physics Research Section B: Beam Interactions with Materials and Atoms*, vol. 172, no. 1, pp. 806 – 811, 2000.

[24] J. T. Wasson and G. W. Kallemeyn, "Compositions of chondrites," *Philosophical Transactions of the Royal Society of London. Series A, Mathematical and Physical Sciences*, vol. 325, no. 1587, pp. 535–544, 1988.

[25] H. Yang and M. Ishiguro, "Evolution of cometary dust particles to the orbit of the earth: Particle size, shape, and mutual collisions," *https://arxiv.org/abs/1801.09332*, 2018.

[26] H. P. Robertson and H. N. Russell, "Dynamical effects of radiation in the solar system," *Monthly Notices of the Royal Astronomical Society*, vol. 97, no. 6, pp. 423–437, 1937.

[27] J.-C. Liou, H. A. Zook, and A. Jackson, "Orbital evolution of retrograde interplanetary dust particles and their distribution in the solar system," *Icarus*, vol. 141, no. 1, pp. 13 – 28, 1999.

[28] J. A. Burns, P. L. Lamy, and S. Soter, "Radiation forces on small particles in the solar system," *Icarus*, vol. 40, no. 1, pp. 1 – 48, 1979.

[29] J. M. Gómez-Guzmán, S. Bishop, T. Faestermann, N. Famulok, L. Fimiani, K. Hain, S. Jahn, G. Korschinek, P. Ludwig, and D. Rodrigues, "Accretion rate of extraterrestrial 41ca in antarctic snow samples," *Nuclear Instruments and Methods in Physics Research Section B: Beam Interactions with Materials and Atoms*, vol. 361, pp. 620 – 626, 2015.

[30] T. Vondrak, J. M. C. Plane, S. Broadley, and D. Janches, "A chemical model of meteoric ablation," *Atmospheric Chemistry and Physics*, vol. 8, no. 23, pp. 7015–7031, 2008.

[31] L. Fimiani, D. L. Cook, T. Faestermann, J. M. Gómez-Guzmán, K. Hain, G. Herzog, K. Knie, G. Korschinek, P. Ludwig, J. Park, R. C. Reedy, and G. Rugel, "Interstellar ^{60}fe on the surface of the moon," *Phys. Rev. Lett.*, vol. 116, p. 151104, Apr 2016.

[32] U. Ott, S. Merchel, S. Herrmann, S. Pavetich, G. Rugel, T. Faestermann, L. Fimiani, J. M. Gomez-Guzman, K. Hain, G. Korschinek, P. Ludwig, M. D'Orazio, and L. Folco, "Cosmic ray exposure and pre-atmospheric size of the gebel kamil iron meteorite," *Meteoritics and Planetary Science*, vol. 49, no. 8, pp. 1365–1374, 2014.

[33] K. Ammon, J. Masarik, and I. Leya, "New model calculations for the production rates of cosmogenic nuclides in iron meteorites," *Meteoritics and Planetary Science*, vol. 44, no. 4, pp. 485–503, 2009.

[34] R. Trappitsch and I. Leya, "Cosmogenic production rates and recoil loss effects in micrometeorites and interplanetary dust particles," *Meteoritics and Planetary Science*, vol. 48, pp. 195–210.

[35] D. Rodrigues, A. Negri, C. Balpardo, A. Arazi, T. Faestermann, J. O. Fernandez Niello, L. Fimiani, J. M. Gómez-Guzmán, K. Hain, G. Korschinek, P. Ludwig, and G. V. Martí1, "Extraterrestrial 53mn deposition on earth," *Applied Radiation and Isotopes, submitted*.

[36] J. M. C. Plane, W. Feng, and E. C. M. Dawkins, "The mesosphere and metals: Chemistry and changes," *Chemical Reviews*, vol. 115, no. 10, pp. 4497–4541, 2015. PMID: 25751779.

[37] L. Megner, M. Rapp, and J. Gumbel, "Distribution of meteoric smoke - sensitivity to microphysical properties and atmospheric conditions," *Atmospheric Chemistry & Physics*, vol. 6, pp. 4415–4426, 2006.

[38] O. Kalashnikova, M. Horanyi, G. Thomas, and O. B. Toon, "Meteoric smoke production in the atmosphere," vol. 27, 2000.

[39] J. Jones and T. R. Kaiser, "The effects of thermal radiation, conduction and metoriod heat capacity on meteoric ablation," *Monthly Notices of the Royal Astronomical Society*, vol. 133, no. 4, pp. 411–420, 1966.

[40] S. Taylor, J. H. Lever, and R. P. Harvey, "Accretion rate of cosmic spherules measured at the south pole," *Nature*, vol. 392, pp. 899–903, 1998.

[41] W. Haynes, *CRC Handbook of Chemistry and Phsics*. Taylor and Francis, 2014-2015.

[42] D. W. Hughes, "Meteors and cosmic dust," *Endeavour*, vol. 21, no. 1, pp. 31 – 35, 1997.

[43] W. J. McNeil, S. T. Lai, and E. Murad, "Differential ablation of cosmic dust and implications for the relative abundances of atmospheric metals," *Journal of Geophysical Research: Atmospheres*, vol. 103, no. D9, pp. 10899–10911, 1998.

[44] I. Langmuir, "The Vapor Pressure of Metallic Tungsten," *Physical Review*, vol. 2, pp. 329–342, Nov. 1913.

[45] C. G. Bardeen, O. B. Toon, E. J. Jensen, D. R. Marsh, and V. L. Harvey, "Numerical simulations of the three-dimensional distribution of meteoric dust in the mesosphere and upper stratosphere," *Journal of Geophysical Research: Atmospheres*, vol. 113, no. D17, 2008.

[46] L. Lanci and B. Delmonte, "Magnetic properties of aerosol dust in antarctic ice cores as a proxy for dust provenance," pp. 2239–, 04 2012.

[47] "Location of the Kohnen stationkartenbasis: Wikimedia / nasa." `https://www.awi.de/expedition/stationen/kohnen-station.html`. Accessed: 2018-3-3.

[48] F. Schrenk, "Ion-chromatographic separation of Chromium and Manganese," bachelor thesis, Technical Universality of Vienna, 2018.

[49] R. Sayer, "Semi-empirical formulas for heavy-ion stripping data," *Revue de Physique Appliquee*, vol. 12(10), p. 1543, 1977.

[50] K. Knie, T. Faestermann, and G. Korschinek, "Ams at the munich gas-filled analyzing magnet system gams," *Nuclear Instruments and Methods in Physics Research Section B: Beam Interactions with Materials and Atoms*, vol. 123, no. 1, pp. 128 – 131, 1997.

[51] R. Lutter, O. Schaile, K. Schöffel, K. Steinberger, P. Thirolf, and C. Broude., "Marabou- a mbs and root based online/offline utility," *Proceedings of the 11th IEEE Real Time Conference*, pp. 14–18, 1999.

Acknowledgements